TOWARD CONVECTIVE-SCALE PREDICTION WITHIN THE NEXT GENERATION GLOBAL PREDICTION SYSTEM

Linjiong Zhou, Shian-Jiann Lin, Jan-Huey Chen, Lucas M. Harris, Xi Chen, and Shannon L. Rees

The variable-resolution version of a Finite-Volume Cubed-Sphere Dynamical Core (FV3)-based global model improves the prediction of convective-scale features while maintaining skillful global forecasts.

Prediction of convective-scale storms has been traditionally performed with regional prediction systems (Weisman et al. 2008; Xue et al. 2013; Clark et al. 2016; Yano et al. 2018). Although issues related to the limited-area domain and boundary conditions remain significant challenges for regional models, convection is poorly represented by low-resolution global prediction systems (Arakawa 2004; Randall 2013). With the rapid increase of supercomputer capacities, innovation of dynamical core algorithms, and improvements in the understanding and representation of physical processes, the resolution gap between regional models and global models is narrowing, and global prediction systems are projected to approach convection-allowing resolutions within the next decade (Stensrud et al. 2009; Yano et al. 2018). A global convection-permitting model without the limitations imposed by local bounded domains (Staniforth 1997; Warner et al. 1997) is potentially more advantageous for mesoscale prediction (Miura et al. 2007; Fudeyasu et al. 2008; Satoh et al. 2008; Putman and Suarez 2011; Miyamoto et al. 2013).

The physical parameterizations and data assimilation techniques of the National Centers for Environmental Prediction's (NCEP) flagship Global Forecast System (GFS) have been continually updated with concomitant improvements in model skill (e.g., Kalnay 2003; www.emc.ncep.noaa.gov/gmb/STATS/html/model_changes.html). However, the hydrostatic spectral dynamical core of the GFS [Global Spectral Model (GSM); Sela 1980], even with continued

AFFILIATIONS: Zhou and X. Chen—Program in Atmospheric and Oceanic Sciences, Princeton University, and NOAA/Geophysical Fluid Dynamics Laboratory, Princeton, New Jersey; Lin and Harris—NOAA/Geophysical Fluid Dynamics Laboratory, Princeton, New Jersey; J.-H. Chen and Rees—University Corporation for Atmospheric Research, and NOAA/Geophysical Fluid Dynamics Laboratory, Princeton, New Jersey
CORRESPONDING AUTHOR: Linjiong Zhou, linjiong.zhou@noaa.gov

The abstract for this article can be found in this issue, following the table of contents.
DOI:10.1175/BAMS-D-17-0246.1

In final form 7 March 2019

improvements in the spatial resolution, energy conservation, and computational efficiency (Juang 2004, 2008; Eckermann 2009; Yang 2009), has not been substantially upgraded since the 1980s. In 2015, the horizontal resolution of the GFS was increased to a grid spacing of 13 km, approaching the commonly accepted limit of 10 km at which the hydrostatic approximation is considered valid. Although a global nonhydrostatic spectral model is theoretically feasible (Juang 1992), the poor scalability makes it impractical for future computing architectures. As a result, it is generally not considered a viable solution to extend the GFS spectral dynamical core to nonhydrostatic scales for the prediction of convective-scale events which requires grid spacing of less than 4 km (Weisman et al. 1997; Done et al. 2004; Roberts and Lean 2008; Prein et al. 2015).

After Hurricane Sandy caused nearly $70 billion in damage and 233 fatalities in the United States and Caribbean nations in 2012, the National Oceanic and Atmospheric Administration (NOAA) initiated the Next Generation Global Prediction System (NGGPS) project with the goal of replacing its global and regional prediction systems with a single unified system to improve its weather prediction capabilities. The NGGPS project provides the means for evaluation and continued development of this system with the goal to make NOAA's global and hurricane forecast guidance the best in the world.

In 2016, the Finite-Volume Cubed-Sphere Dynamical Core (FV3), developed at the NOAA/Geophysical Fluid Dynamics Laboratory (GFDL), was selected as the dynamical core of NGGPS to replace the GSM. FV3 was chosen for its high efficiency and scalability; its run-time switchable nonhydrostatic solver, allowing convective-scale simulation; its exact mass and approximate energy conservation; its skillful forecasts and adaptability to the present GFS physics and data assimilation system; and its robust kinetic energy spectrum, demonstrating an excellent match to synoptic-to-mesoscale observations (www.weather.gov/sti/stimodeling_nggps_implementation_atmdynamics).

During the dynamical core evaluation period, GFDL scientists developed a new global model coupling the FV3 with GFS physical parameterizations, which later became the prototype of NGGPS. This model is called the finite-volume Global Forecast System, or fvGFS. The fvGFS was later transitioned to NCEP for further incorporation into GFS's existing modeling architecture which allowed more comprehensive verification and validation. The new prediction system has demonstrated broadly superior performance compared to the current operational GFS (https://vlab.ncep.noaa.gov/web/fv3gfs). At GFDL, a research version of fvGFS is being continuously developed and maintained with new and enhanced features including the capability of convective-scale prediction.

The nonhydrostatic dynamics in the FV3 allow the fvGFS to run globally at resolutions high enough to explicitly simulate convective-scale motions (Lin 2018). However, present-day computing resources are insufficient to support real-time global convective-scale weather prediction. Variable-resolution capabilities within the FV3 allow a high-resolution region within the global domain, which enables the model to efficiently reach higher resolutions with fewer disadvantages inherent in limited-area models. One such method, grid stretching (Fox-Rabinovitz et al. 2006; McGregor 2015; Harris et al. 2016), smoothly deforms the cubed sphere, refining the domain over a region of interest while creating a relatively coarse region on the opposite side of Earth. The stretched grid is topologically identical to the original cubed sphere and yields a much smoother transition from the coarse-resolution global grid to the high-resolution region when compared to the abrupt transition and multiple domains of the nested configuration (Harris and Lin 2013).

Although the stretched fvGFS enables convective-scale prediction at lower cost, the present physical parameterizations built for the 13-km GFS still limit the forecast skill. Several studies have shown that parameterized convection, cloud microphysics, and boundary layer diffusion need to be modified to allow realistic high-resolution simulations (Weisman et al. 2008; Baldauf et al. 2011; Clark et al. 2016). Cloud microphysics are particularly sensitive to resolution (Bryan and Morrison 2012), and they are the most important processes for convective-scale simulations. The Zhao–Carr cloud microphysics (Zhao and Carr 1997) used in the operational GFS is known to be deficient for cloud-resolving models (Li et al. 2005), and a more advanced cloud microphysics scheme is necessary for realistic convective-scale simulation.

In this study, we use a version of fvGFS developed at GFDL to perform convective-scale prediction by adopting the FV3 and its stretched grid approach to reach a 4-km resolution over the contiguous United States (CONUS). The convective-scale prediction is improved by implementing an upgraded six-category cloud microphysics scheme. The goal of this study is to demonstrate that the fvGFS can maintain skillful forecasts in the global domain and simultaneously produce a higher-quality prediction of continental convective phenomena than is possible at the resolution of current operational global models.

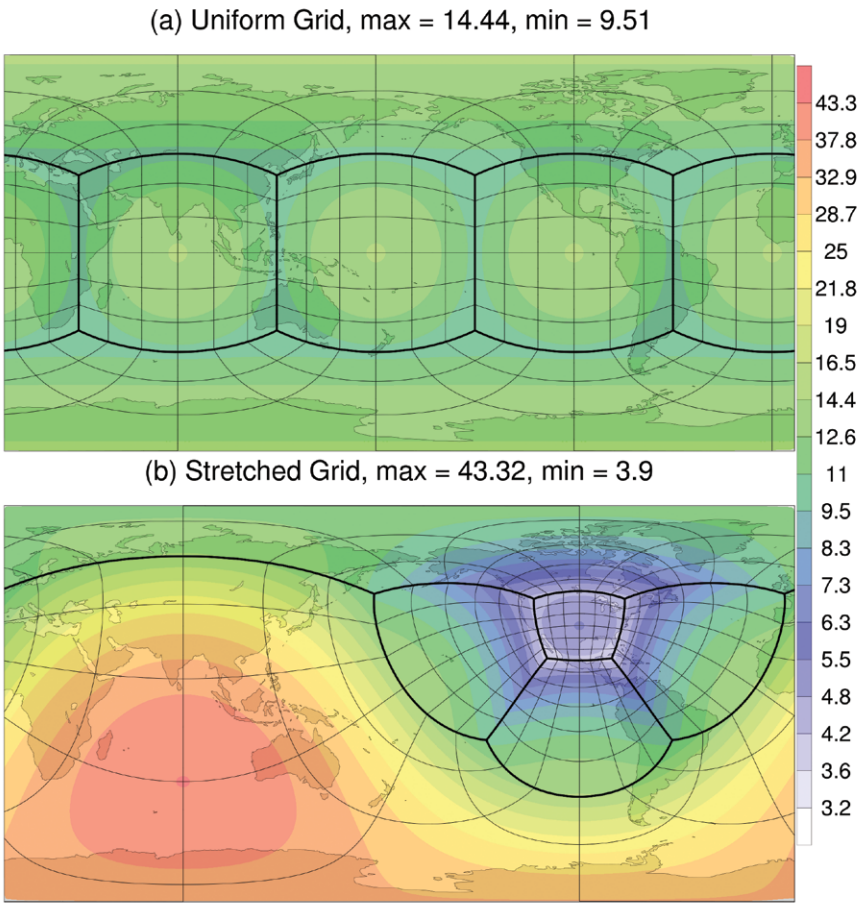

Fig. 1. Local gridcell widths (shading, units: km, estimated as the square root of the cell area) in fvGFS configurations. (a) (quasi) Uniform grid and (b) stretched grid centered at Oklahoma City. The maximum and minimum values (units: km) of the gridcell widths are in the header of each panel. Thick lines are the boundaries of cubed-sphere tiles, and thin lines are the boundaries of grid cells (plotted every 128 × 128 cells).

MODEL AND METHODS. The fvGFS model, which couples the FV3 dynamical core to the common GFS physics package, was initially developed during the NGGPS phase II for the evaluation of dynamical cores under a wide range of realistic atmospheric initial conditions. Since mid-2016, the 13-km uniform-resolution version of the fvGFS has been running in real time at GFDL. The forecast characteristics of the fvGFS, with a focus on tropical cyclone prediction, have been described in Chen et al. (2019) with refinement to convective scales reported in Hazelton et al. (2018a,b).

The FV3 in fvGFS uses the "vertically Lagrangian" dynamics of Lin (2004) extended with the nonhydrostatic pressure gradient computation of Lin (1997) and a semi-implicit solver for vertically propagating sound waves, discretized on the cubed-sphere grid of Putman and Lin (2007). The explicit version of the vertically Lagrangian nonhydrostatic discretization is described in Chen et al. (2013) within an unstaggered grid. GFS physical parameterizations include simplified Arakawa–Schubert (SAS) shallow and deep convection (Han and Pan 2011), Zhao–Carr gridscale condensation and precipitation (Zhao and Carr 1997), orographic and convective gravity wave drag (Chun and Baik 1994; Kim and Arakawa 1995; Kim and Doyle 2005), boundary layer vertical diffusion (Han et al. 2016), and the Rapid Radiative Transfer Model (RRTM; Clough et al. 2005). The Noah land surface model (Ek et al. 2003) provides land surface interactions. Initialization of the atmosphere, land, and sea surface temperatures is taken directly (i.e., cold started) from the NCEP operational global model analyses.

In this study, the fvGFS model was initially built on a 13-km (quasi) uniform global grid (Fig. 1a), and subsequently developed on the same grid stretched by a factor of 3, centered in the United States at Oklahoma City (35.4°N, 97.6°W; Fig. 1b). In the stretched-grid configuration, horizontal grid spacing varies smoothly from 4 km over the CONUS to 45 km at the antipodal point over the Indian Ocean. This deformation has the same number of grid cells as the 13-km uniform grid. A horizontal resolution of 4 km is considered to be convection permitting, that is, the resolution at which the model starts to resolve convection, as summarized by Prein et al. (2015, and references therein).

Initially, both the uniform-grid and stretched-grid fvGFS use the same parameters except for the time steps. For the 13-km uniform grid (Uniform_ZC in Table 1), the acoustic time step is 18.75 s, and the dynamics and physics time steps are both 150 s. For the 4–45-km stretched grid (Stretched_ZC in Table 1), 5-, 25-, and 75-s time steps are used, owing to the

more stringent time step restriction in the high-resolution region. Using these shorter time steps and same resources, Stretched_ZC needs about 2 times more wall clock to complete a 10-day forecast compared to Uniform_ZC. The U.S. Geological Survey (USGS) 30-s-resolution terrain dataset (Gesch et al. 1999) is utilized to compute mean terrain height, standard deviation, and gravity wave drag (GWD)-related parameters on the native cubed-sphere grid. The physics package used in these two fvGFS versions is largely the same as the operational GFS. However, the GWD in the fvGFS is adjusted accordingly. Additionally, to improve the simulation of moist processes and especially of convective-scale clouds, the Zhao–Carr cloud microphysics (hereafter ZC MP; Zhao and Carr 1997) is replaced with the GFDL single-moment 6-category cloud microphysics (hereafter GFDL MP; see the appendix) upgraded from Chen and Lin (2011, 2013). In this study, Stretched_G (Table 1) is short for the stretched-grid fvGFS using GFDL MP. Note that the cumulus parameterization scheme is applied to Stretched_G globally, because the grid spacing required to resolve convection adequately is debatable (Bryan et al. 2003; Petch 2006), and the SAS deep convection is still applicable and has been shown to produce improved simulations at 2-km resolution (Hazelton et al. 2018b).

Table 1. Characteristics of the fvGFS configurations. The three configurations differ in their resolutions, time steps, and microphysics but are otherwise identical.

Model ID	Resolution	Cloud microphysics
Uniform_ZC	13-km (quasi) uniform grid	Zhao–Carr
Stretched_ZC	4–45-km stretched grid	Zhao–Carr
Stretched_G	4–45-km stretched grid	GFDL

Using the same initial conditions as the operational GFS, we performed 145 ten-day forecasts initialized at 0000 UTC every 5 days, for each fvGFS configuration, covering the period from 16 January 2015 to 11 January 2017. The 17 March 2016 case is excluded due to missing forecast data for the operational GFS. The interpolation procedure to convert data from the GFS Gaussian grid to the cubed-sphere grid is documented in Chen et al. (2018). This study uses the European Centre for Medium-Range Weather Forecasts (ECMWF) interim reanalysis (ERA-Interim; 0.75°; Dee et al. 2011), the NCEP–NCAR reanalysis (1°; Kalnay et al. 1996), Stage IV radar-derived precipitation (4 km; Lin 2011), and observed radar reflectivity (5 km) for verification of the forecasts. Results from the operational GFS, on a Gaussian grid with nominal 13-km resolution, are used as a baseline for direct comparison.

The forecast skill is assessed with several statistical quantities. The anomaly correlation coefficient (ACC) is the most commonly used metric for global (large scale) forecasts and quantifies the correlation between the predicted and observed anomalies (Jolliffe and Stephenson 2003). The calculation of ACC uses an ERA-Interim reanalysis for verification and NCEP–NCAR reanalysis for climatology (Murphy and Epstein 1989). To verify precipitation forecasts, the equitable threat score (ETS) and bias score (BIAS; Hamill 1999), relative operating characteristics (ROC; Mason and Graham 1999), and fractions skill score (FSS; Roberts and Lean 2008) are employed. These four statistical scores have been widely used in assessing precipitation forecasts throughout the mesoscale prediction community (Done et al. 2004; Stephan et al. 2008; Weisman et al. 2008; Schwartz et al. 2010; Sobash et al. 2011; Xue et al. 2013; Schumacher and Clark 2014; Müller et al. 2017). In this study, the 95% confidence interval is calculated using the Student's t test: $z_{1-a/2}sn^{-1/2}$, where z is the critical value of the Student's t distribution, $a = 0.05$ is confidence level, s is the standard deviation, and n is the sample size.

LARGE-SCALE FORECAST. Accurate prediction of the large-scale circulation is essential to a global prediction system because it determines the environment for synoptic-scale and convective-scale processes that govern the local weather. A critical measure for assessing the quality of the large-scale forecast skill is the 500-hPa geopotential height (H500 for short hereafter). This section presents verifications for the 10-day evolution of H500 ACCs for the GFS and the fvGFS with the three configurations.

As expected the H500 ACCs for all models monotonically drop from nearly 1.0 at hour 6 to about 0.4 by day 10 (Figs. 2a–c), indicating that the prediction becomes less skillful as the lead time increases. Compared to the GFS, Uniform_ZC's ACC is slightly lower in the first 8 days (Figs. 2d–f), which implies changing only the dynamical core without reconfiguring the physics degrades the forecast skill. However, the degradation is insignificant. Not surprisingly, Stretched_ZC's forecast skill significantly degrades in both the Northern Hemisphere in the first 7 days and the Southern Hemisphere in the first 8 days due to the coarse resolution in the Euro-Asian and African continents, and in the Southern Hemisphere (Fig. 1b).

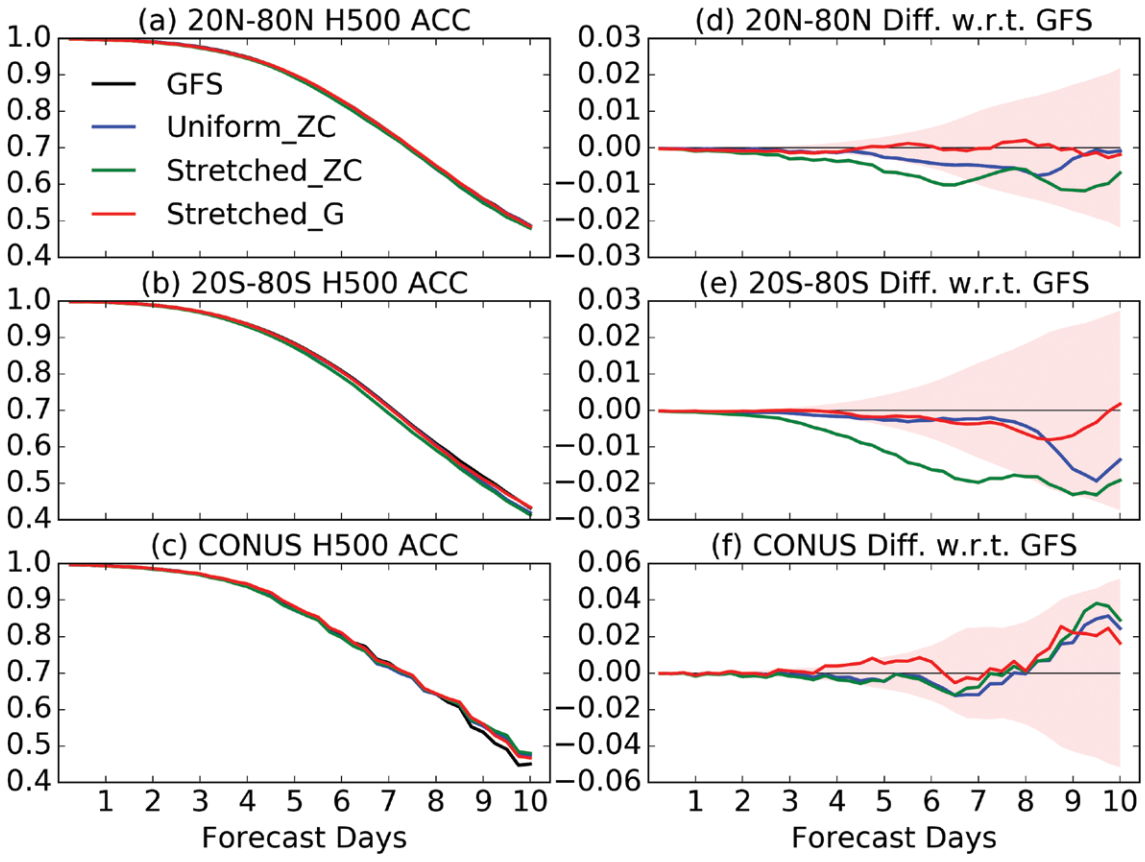

Fig. 2. "Die off" plots of 145-case-mean H500 ACCs for the GFS and the fvGFS configurations: (a) Northern Hemisphere, (b) Southern Hemisphere, and (c) CONUS. (d)–(f) Difference relative to GFS, with the 95% confidence interval shown as pink shading.

After switching from ZC MP to GFDL MP in the stretched-grid fvGFS (Stretched_G), the forecast skill improves for both hemispheres and the CONUS. Stretched_G shows performance comparable to the GFS in the Northern Hemisphere for the entire 10-day forecast but is slightly worse in the Southern Hemisphere, likely due to the degraded resolution. Over the CONUS, Stretched_G ACC is about 0.01 higher than the fvGFS using ZC MP (both Uniform_ZC and Stretched_ZC) between day 4 and day 7. These results strongly suggest that an upgraded physical parameterization is important for improving the prediction skill of the large-scale circulation when the local resolution is enhanced. Since use of the more comprehensive cloud microphysics scheme results in greatly improved prediction skill, and the performance of Stretched_ZC is unacceptable, the following discussion will not include the results of Stretched_ZC.

CONVECTIVE-SCALE PREDICTION: MULTICASE STATISTICS. This section presents verifications of convective-scale prediction over the CONUS, where the grid spacing is about 4 km. The orographic precipitation, quantitative precipitation forecast, the diurnal cycle of precipitation, and the probability distribution function of precipitation are verified over the 2-yr period. For convective-scale prediction, the forecasts beyond 5 days are generally much less skillful. Therefore, this section focuses on the first 5 days of each forecast. All verifications are conducted based on the observation and model output interpolated onto the same 4-km resolution grid.

Orographic precipitation. With higher resolution over the CONUS in the stretched grid configuration, the complex terrain such as the Rocky and Appalachian mountain ranges is resolved much better, as well as small-scale convection. Comparing the 145-case averaged precipitation of the GFS, Uniform_ZC, and Stretched_G with the Stage IV observations (Fig. 3), the benefit of higher resolution on precipitation simulation is evident. Spectral dynamical cores have difficulty simulating fields with sharp spatial gradients or discontinuities (Gibbs phenomenon), which results in noisy precipitation patterns in the operational GFS (Fig. 3c). By contrast, the fvGFS simulations do not present any

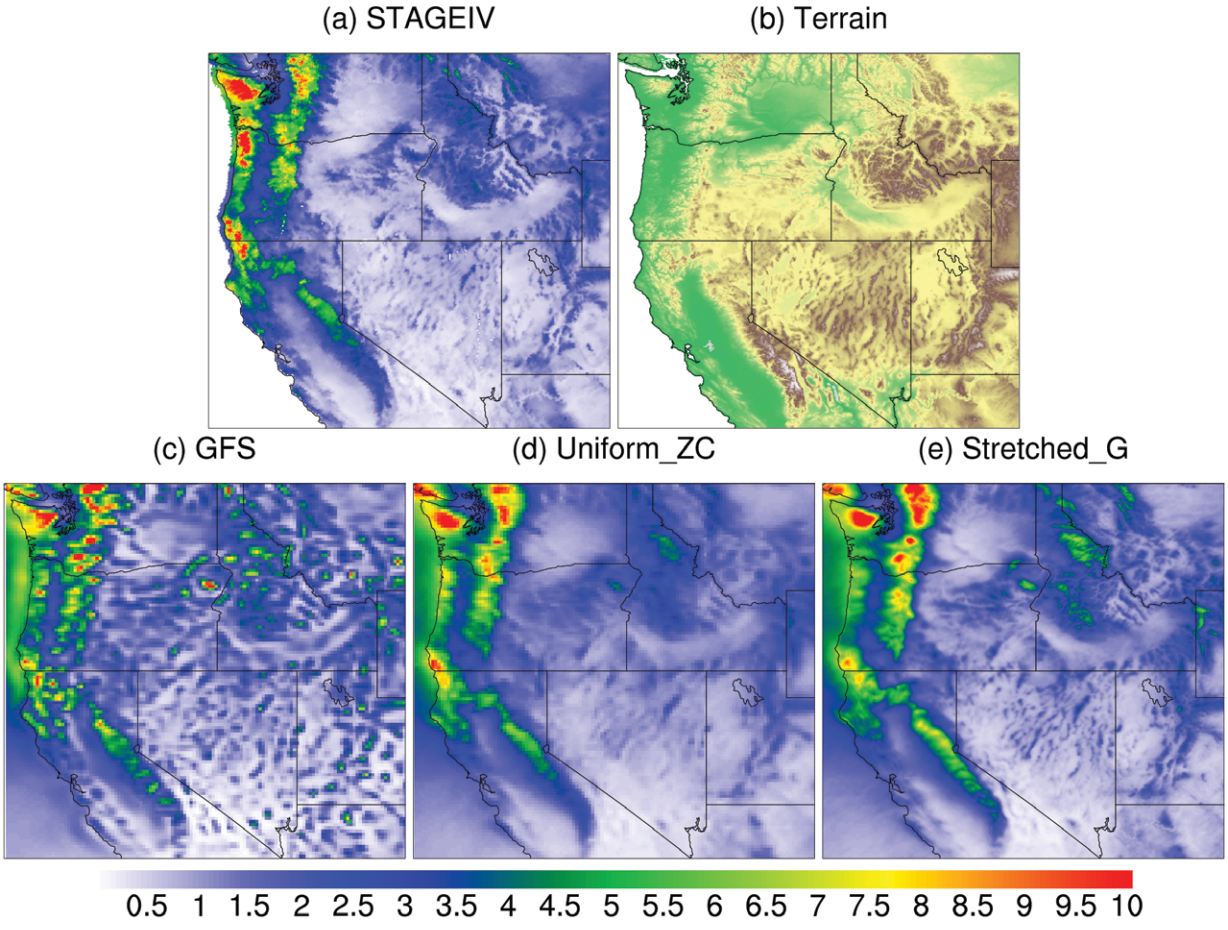

Fig. 3. Geographical distribution of 145-case averaged precipitation rate (mm day^{-1}): (a) Stage IV observations, (c) GFS, (d) Uniform_ZC, and (e) Stretched_G. (b) Terrain elevation ranging from 0 (green) to 3,800 m (brown).

Gibbs-ringing-type noise, while Stretched_G simulations show a broadly improved representation of small-scale orographic precipitation details compared to the 13-km simulations (Figs. 3d,e). However, the fvGFS, especially the locally high-resolution stretched-grid version, underestimates the precipitation along the west coast of Oregon and overestimates the precipitation along the Cascade Mountains (Figs. 3d,e). This bias has been widely documented in the literature for other numerical models (Mass et al. 2002, and references therein). To better predict the orographic precipitation, a subgrid terrain-adjusted cloud microphysics parameterization may be required (Leung and Ghan 1998).

Quantitative precipitation forecast. The quantitative precipitation forecast skill over the CONUS region is computed for all 145 five-day forecasts and presented in Fig. 4. For the first 1–3-day forecast period, the ETS (higher values indicate greater skill; with 1.0 representing a perfect forecast) for the GFS peaks at the 2 mm day^{-1} threshold (Fig. 4a) and gradually decreases in skill for more intense (and rarer) precipitation events (solid line). The prediction of light precipitation (less than 2 mm day^{-1}) in the GFS is relatively less skillful. Compared to the GFS, Uniform_ZC and Stretched_G show distinctively higher ETS for the 1–3-day forecasts, with Stretched_G exhibiting the highest ETS for light precipitation. The improvement of light precipitation in Stretched_G is possibly due to the use of the GFDL cloud microphysics, which results in a more consistent dynamics–physics coupling (see the appendix).

Figures 4b and 4c show the differences in ETS between the two fvGFS versions and the GFS. Compared to the GFS, Uniform_ZC displays significantly higher ETS from the 0.2 to 35 mm day^{-1} precipitation thresholds during the first 1–3-day forecast period (Fig. 4b), indicating that Uniform_ZC is notably better in the prediction of light to moderate precipitation in a short-term forecast period. For the 4–5-day forecasts, Uniform_ZC still presents higher ETS than the GFS (Fig. 4c), but the difference between them is insignificant except for the light precipitation (0.2 mm day^{-1}). After grid stretching and updating to GFDL MP, Stretched_G increases ETS for both light

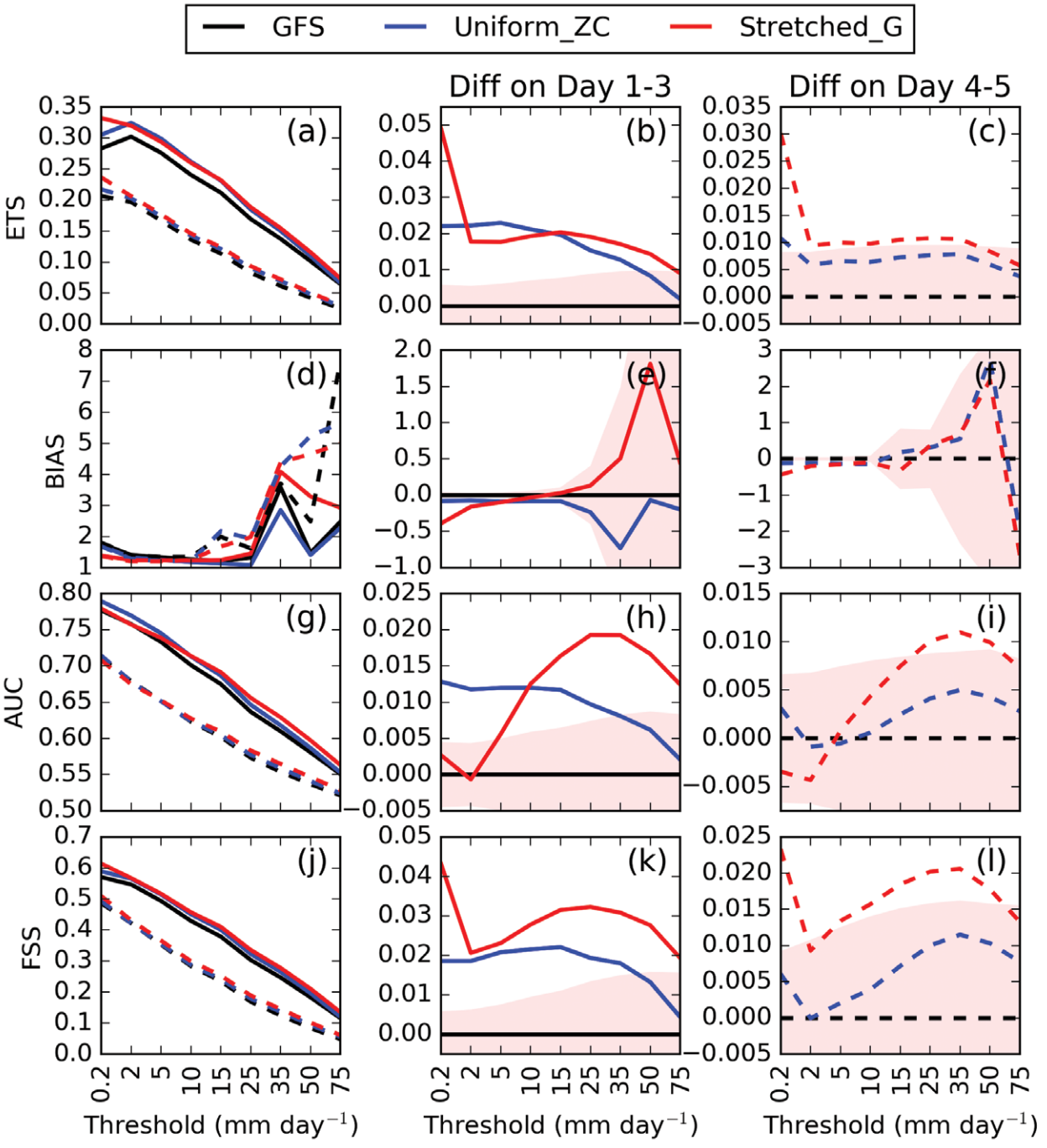

Fig. 4. (a) The ETS of precipitation over CONUS as a function of precipitation threshold for the operational GFS model (black), Uniform_ZC (blue), and Stretched_G (red), averaged over days 1–3 (solid) and 4–5 (dashed) of the forecast. (b) ETS difference relative to GFS over days 1–3. (c) ETS difference relative to GFS over days 4–5. Colors of lines in (b) and (c) are the same as in (a). (d)–(f) As in (a)–(c), but for BIAS. (g)–(i) As in (a)–(c), but for the area under the AUC. (j)–(l) As in (a)–(c), but for the FSS. Pink shading indicates the 95% confidence interval for the differences to GFS.

and heavy precipitation during the 1–3-day forecast period (Fig. 4b). As a result, the improvement relative to the GFS is significant for the entire precipitation range. Compared to Uniform_ZC, a distinct improvement is shown in Stretched_G for the 4–5-day forecasts (Fig. 4c). The difference from the GFS for precipitation thresholds below 35 mm day^{-1} is statistically significant at the 95% confidence level.

Figure 4d presents the BIAS of all three models. A BIAS greater (less) than 1 indicates an overestimation

(underestimation) of precipitation. A BIAS greater than 1 also indicates that there are many more places where extreme precipitation is forecasted than where they actually occur. As can be seen from Fig. 4d, both the GFS and the two versions of fvGFS overestimate the precipitation (BIAS > 1) during the entire 5 days, especially for precipitation amounts greater than 25 mm day^{-1}. This implies that all these models are less skillful in predicting the exact location of the heavy to extreme precipitation. Stretched_G demonstrates significant improvements in the prediction of light precipitation of less than 2 mm day^{-1} (Fig. 4e), which is consistent with the ETS result at the 0.2 mm day^{-1} precipitation threshold. For heavy precipitation, the Stretched_G's BIAS is insignificantly higher than the GFS's BIAS, which implies that the Stretched_G's configuration is still underoptimized for heavier precipitation intensity. Modifications to other physical parameterizations (including the planetary boundary layer parameterization) may be necessary at convection-permitting scales to address these issues. For the 4–5-day forecast period, the differences among these models are mostly within the 95% confidence level, except for very light precipitation.

Hamill (1999) pointed out that ETS is sensitive to precipitation bias. As our analysis of ETS and BIAS shows a similar sensitivity, we employ ROC to perform an unbiased precipitation verification. The area under the ROC curve (AUC) is shown in Figs. 4g–i. AUC values range from 0 to 1.0 with a higher value indicating a higher hit rate for the precipitation events. Figure 4g shows a similar trend of the Stretched_G's AUC as seen in the ETS (Fig. 4a). However, the difference between the Stretched_G and the GFS (Fig. 4h) is different from that shown in Fig. 4b. Compared to the GFS, the AUC for the Stretched_G shows little improvement in the prediction of light precipitation (less than 5 mm day^{-1}). These results demonstrate that the improvements in the ETS shown in Fig. 4b are mainly due to the significant reduction of light precipitation bias shown in Fig. 4e. By contrast, Stretched_G shows much higher AUC for moderate to heavy precipitation amounts (greater than 15 mm day^{-1}) while the difference in BIAS is insignificant (Fig. 4e). This indicates that the improvement in the forecast of moderate to heavy precipitation amounts is mainly due to the variability instead of the bias. In the 4–5-day forecast period (Fig. 4i), the AUC for light to moderate precipitation drops considerably for both Uniform_ZC and Stretched_G, and the differences relative to the GFS are mostly insignificant.

Note that in these verifications there was no consideration of small positioning differences in the computation of ETS, BIAS, and AUC. Therefore, when the locations of intense forecast precipitation structures are shifted relative to the observed locations, the forecast skill of the model may not be well represented by these metrics (Clark et al. 2009). The FSS is used to verify precipitation forecasts in an 8×8 km^2 neighborhood (Fig. 4j). The FSS ranges from 0 to 1, where a higher FSS means that the model can better predict the precipitation probability in a particular neighborhood area. It is seen in Fig. 4j that the FSS along the range of precipitation thresholds shows a similar trend to ETS as shown in Fig. 4a. Figure 4k shows similar FSS differences to those for ETS in Fig. 4b in the 1–3-day forecast period, compared to the GFS. One exception is Stretched_G, which has a higher FSS than Uniform_ZC for the entire precipitation intensity range. This indicates that the higher-resolution fvGFS is more skillful in predicting the precipitation probability in a targeted neighborhood. For the 4–5-day forecast period (Fig. 4l), the difference in FSS for Uniform_ZC relative to the GFS is within the 95% level of confidence, while Stretched_G shows significantly higher FSS than the GFS for almost the entire precipitation range.

The diurnal cycle of precipitation. Prein et al. (2015) concluded that a primary added value in convection-permitting simulations is an improved diurnal cycle of precipitation. This subsection verifies the diurnal cycle of precipitation over the CONUS following Bechtold et al. (2014) and Zhou et al. (2015). Figure 5 shows the diurnal phase [local standard time (LST)] and diurnal amplitude (mm day^{-1}) of 3-hourly precipitation from Stage IV, the GFS, and the two fvGFS versions for all of 2015 and 2016. In Fig. 5a, the diurnal phase of the Stage IV observations exhibits distinct patterns in the western, central, and eastern CONUS regions. In the western CONUS, the precipitation peaks primarily in the afternoon (1200–1800 LST), while in the eastern CONUS, it peaks primarily in the late afternoon to evening (1500–2100 LST). In the central CONUS, the peak precipitation occurs mainly in the period from evening to dawn (1800–0600 LST next day).

Among the three models and configurations, Stretched_G is generally the best at reproducing the west-to-east pattern and shows the lowest root-mean-square errors (RMSEs) when compared to the Stage IV observations over the entire CONUS (Fig. 5d). Over the western and eastern CONUS, the Stretched_G times of peak precipitation compare most favorably with the Stage IV observations, while the GFS produces a later time of peak precipitation (Fig. 5b), and Uniform_ZC produces various times of peak precipitation

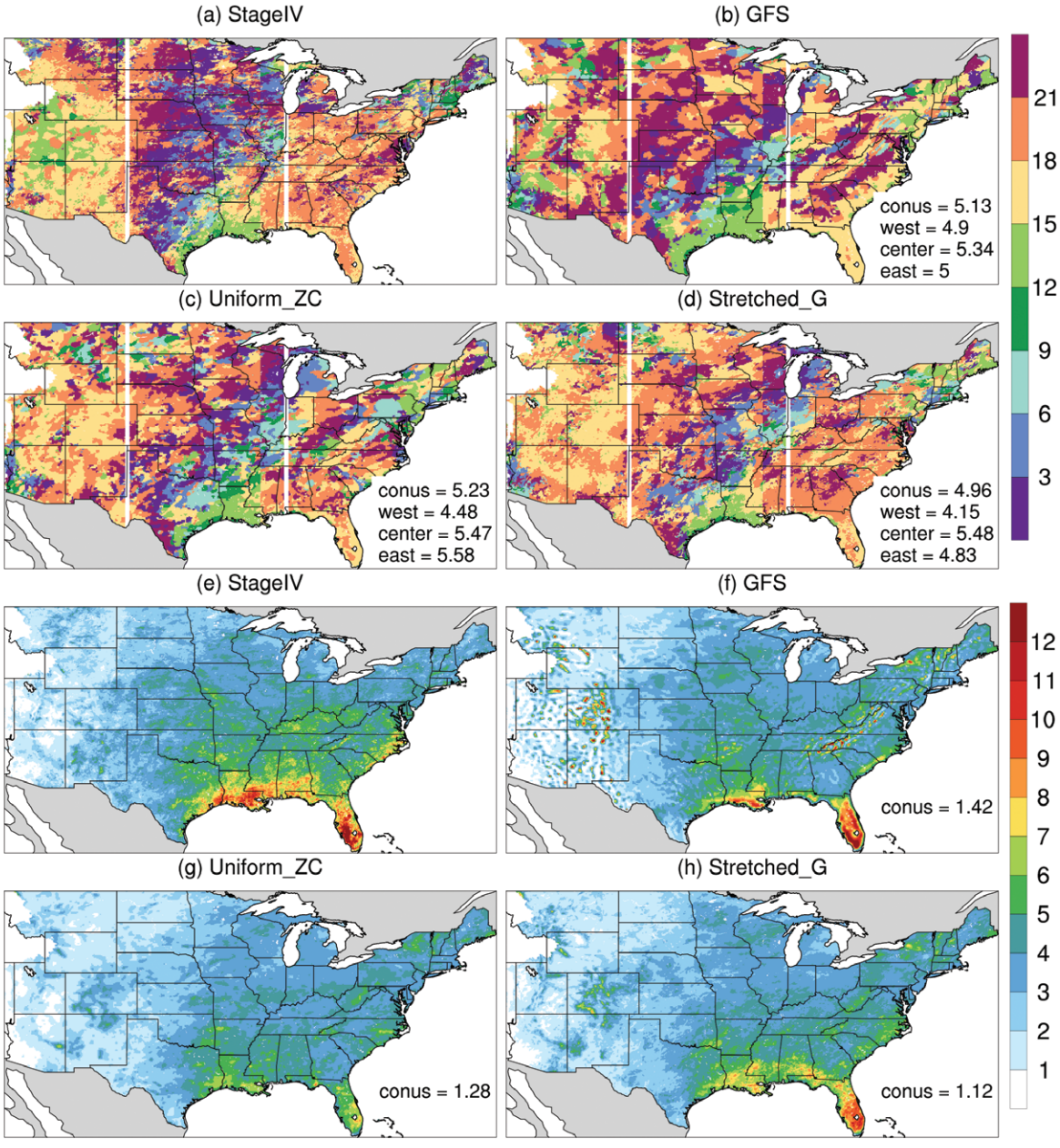

Fig. 5. (a)–(d) Diurnal phase (LST) and (e)–(h) diurnal amplitude (mm day^{-1}) of the precipitation over CONUS as obtained from (a),(e) Stage IV; (b),(f) GFS; (c),(g) Uniform_ZC; and (d),(h) Stretched_G. RMSEs over the CONUS and the western, central, and eastern regions for each simulation are at the right bottom corner of the panels. The white lines in (a)–(d) are the boundaries of western, central, and eastern CONUS regions at 103° and 87.5°W.

(Fig. 5c). However, over the northern part of the central CONUS, the peak time of precipitation for Stretched_G is 3–6 h earlier than observed, indicating that Stretched_G still struggles with representing the self-propagating, diurnally driven convection. Note that the cumulus convective scheme configured for the 13-km GFS is still applied in Stretched_G globally. Previous studies (Davis et al. 2003; Clark et al. 2007) show that cumulus parameterization schemes tend to reduce the representation of precipitation's diurnal cycle. In the future, a scale-aware convective scheme will be considered to address this issue.

The diurnal amplitude of observed precipitation in Fig. 5e shows that the peak precipitation is stronger than 10 mm day^{-1} along the coast of the Gulf of Mexico as well as over Florida. The diurnal amplitude decreases from the southeastern CONUS to the northern and western CONUS region. The GFS reproduces

the intense diurnal amplitude over Florida and the coast of Louisiana, but it fails to produce the intense diurnal amplitude over other coastal areas along the Gulf of Mexico. The GFS also spuriously produces an extreme and noisy diurnal amplitude over the western CONUS and along the Appalachians (Fig. 5f). By contrast, Uniform_ZC underestimates the diurnal amplitude for the southeastern CONUS (Fig. 5g). Its maximum diurnal precipitation amplitude is lower than 8 mm day^{-1}. After grid stretching and updating to GFDL MP, Stretched_G enhances the diurnal amplitude to above 10 mm day^{-1} along the coast of the Gulf of Mexico and over Florida (Fig. 5h). However, the diurnal amplitude of precipitation in Stretched_G is still too weak compared with the Stage IV observations.

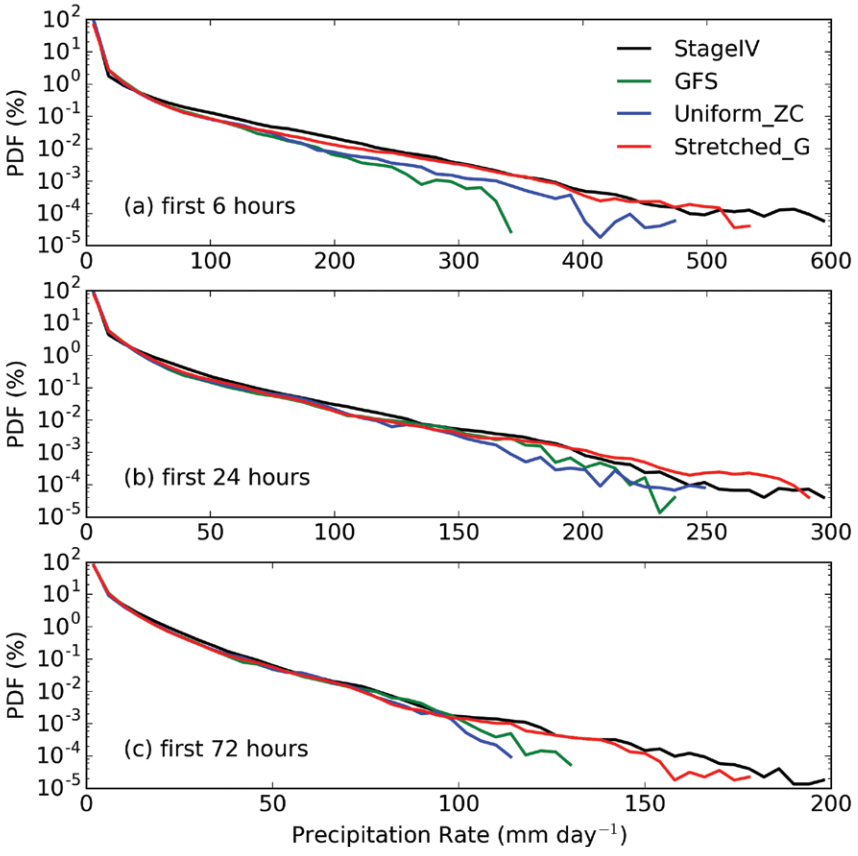

Fig. 6. Probability distribution function (PDF, %) of (a) first 6-h, (b) first 24-h, and (c) first 72-h mean precipitation rate (mm day^{-1}) over SGP as obtained from 145-case Stage IV (black) observations, and GFS (green), Uniform_ZC (blue), and Stretched_G (red) forecasts.

The probability distribution function of precipitation. The southern Great Plains region (SGP; 30°–40°N, 105°–90°W) experiences the most thunderstorms, tornadoes, and other severe weather in the United States (Grams et al. 2012). By analyzing the probability distribution of precipitation in the SGP (Fig. 6), the predicted heavy precipitation in Stretched_G is found to be remarkably close to the Stage IV observations. Both the GFS and Uniform_ZC produce substantially less heavy precipitation compared to observations, and the two models fail to produce precipitation rates higher than 500 mm day^{-1} in the first 6 h, 250 mm day^{-1} in the first 24 h, and 125 mm day^{-1} in the first 72 h. Both versions of the fvGFS are better able to produce intense precipitation rates during the first six hours of the forecast compared to the operational GFS (Fig. 6a), indicating a very rapid spinup from the GFS initial conditions. Stretched_G in particular shows very rapid adjustment from the relatively low-resolution 13-km hydrostatic GFS initial conditions to agree well with the observed probability distribution.

CONVECTIVE-SCALE PREDICTION: CASE STUDIES. Examples of prediction of specific weather events are provided to demonstrate the convection-permitting capability of the fvGFS. This section investigates two different cases: a squall line on 1 May 2017 and Hurricane Harvey on 25 August 2017. The two forecasts are initialized at 0000 UTC 1 May 2017 and 25 August 2017, respectively. The model predicted composite radar reflectivity is diagnosed using Stoelinga's (2005) algorithms in Stretched_G. Since the ZC MP has no prognostic precipitation, simulated reflectivity is not available for the GFS or the Uniform_ZC.

On 1 May 2017, a squall line with associated strong convection developed in the Great Plains area and propagated toward the east coast of the United States. Figure 7a shows the observed major squall line at 0900 UTC 1 May 2017. The 9-h forecast of Stretched_G produces a band of intense radar reflectivity extending from Kentucky into the Gulf of Mexico that agrees well with the observations

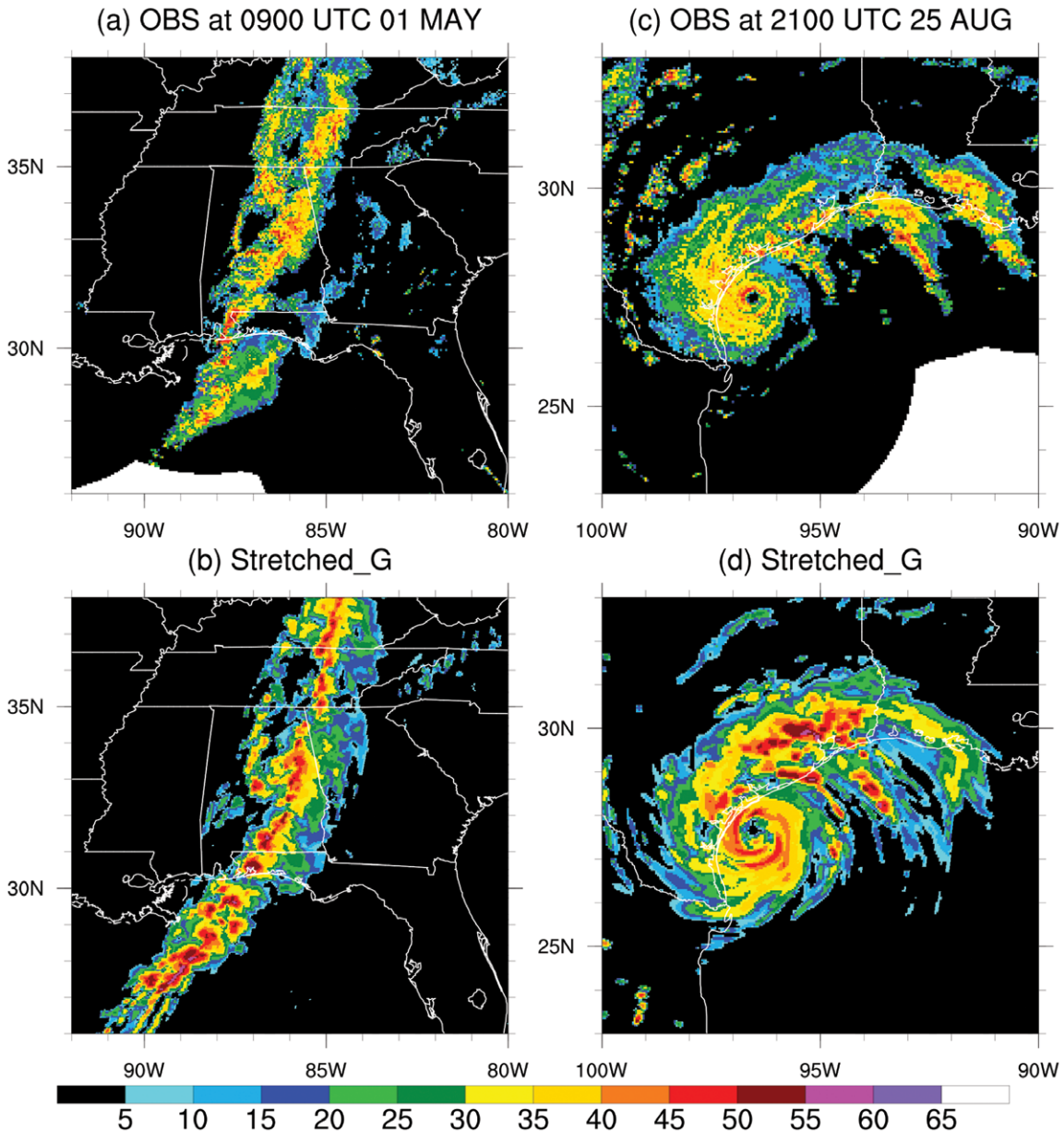

Fig. 7. Composite radar reflectivity (dBZ) of (a),(c) observations, and (b),(d) Stretched_G at (a),(b) 0900 UTC 1 May and (c),(d) 2100 UTC 25 Aug 2017.

(Fig. 7b). The intense radar reflectivity is caused by a large number of narrow and concentrated mesoscale storms along the squall line. Although the locations of these mesoscale storms do not precisely match the observations, the Stretched_G's capability to predict convective-scale features is apparent. The predicted convective-scale storms are generally more intense, and their sizes are slightly larger than observed, especially over the Gulf of Mexico. There are also more pronounced stratiform echoes predicted by the model than observed. These differences imply that the SAS convection scheme, GFDL MP, and boundary layer vertical diffusion may be underoptimized for 4-km resolution.

On 25 August 2017, Hurricane Harvey approached the coast of Texas and started to bring extensive precipitation and flooding to southern Texas and Louisiana. The observed center of the hurricane at 2100 UTC was about 40 miles off the coast, which is correctly predicted by Stretched_G (Figs. 7c,d). The overall observed structure of the spiral rainbands, with embedded mesoscale storms extending out to the northeast of the storm center along the coasts of Texas and Louisiana, is also reproduced very well

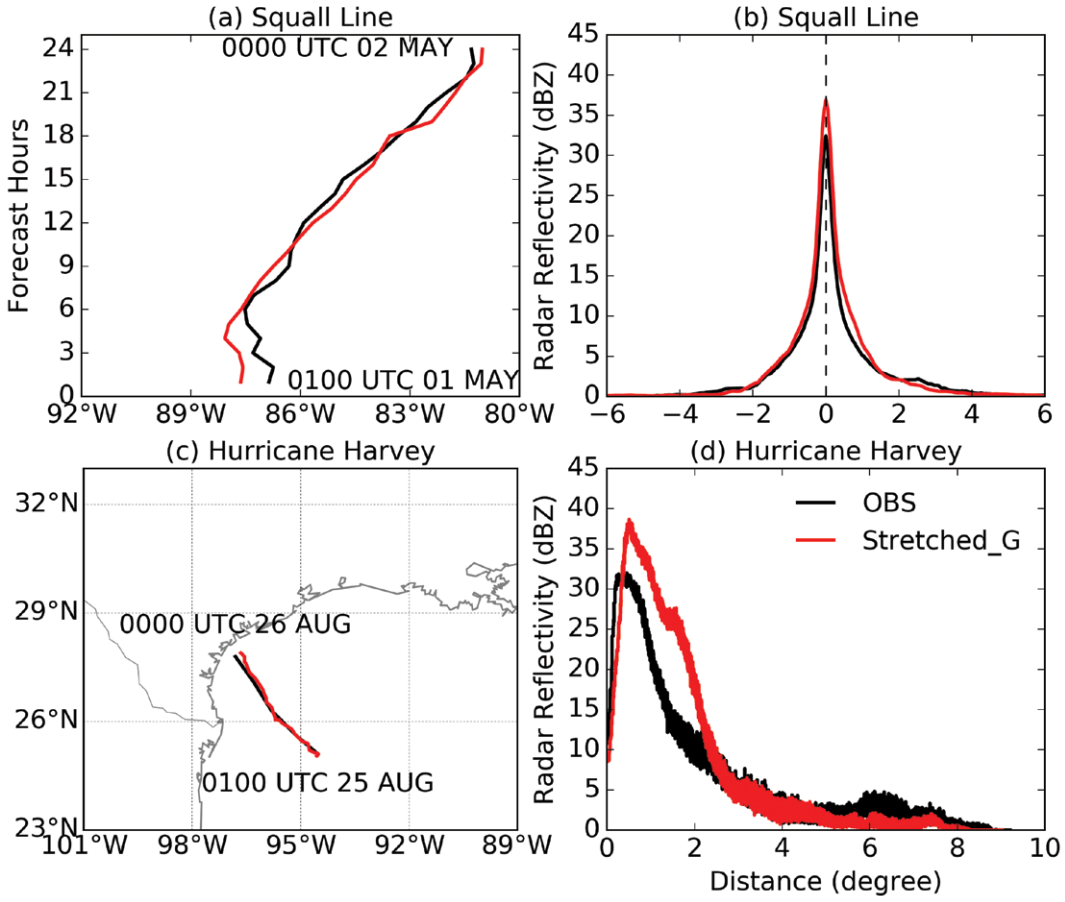

Fig. 8. Comparison of the (a) hourly squall line track from 0100 UTC 1 May to 0000 UTC 2 May 2017, (b) 24-h radar reflectivity composite of the west–east cross section through the squall line on 1 May 2017, (c) hourly Hurricane Harvey track from 0100 UTC 25 Aug to 0000 UTC 26 Aug 2017, (d) 24-h radar reflectivity composite of the inner-core to outer-core cross section through Hurricane Harvey on 25 Aug 2017 between observations (black) and Stretched_G (red).

in the Stretched-G forecast at the lead time of 21 h. However, the forecast locations of the bands are closer to the hurricane center, and the embedded storms are generally stronger than observed, which is similar to what was shown in the squall line case. However, the locations and sizes of these hurricane bands are difficult to predict due to the complex interaction of Harvey with the large-scale circulation and the local moisture environment.

To further evaluate the characteristics of the squall line event simulation, we define the longitudinal center of the squall line as the meridionally averaged zonal maximum of the radar reflectivity in the 26°–38°N, 92°–80°W domain as illustrated in Figs. 7a and 7b. The movement of the longitudinal center of the squall line produces the tracks shown in Fig. 8a. The 24-h radar reflectivity composite of the west–east cross section through the squall line is shown in Fig. 8b, which is calculated as the 24-h average of the radar reflectivity along the longitudinal centers. The track of the squall line predicted by Stretched_G lags about 1° behind the observed squall line in the first 6 h of the forecast. At lead times beyond the 6-h forecast, the predicted track catches up and almost aligns with the observed squall line track through 24 h. Stretched_G correctly simulates the shape of the mesoscale convective elements across the squall line (Fig. 8b), although the intensities are about 2–5 dBZ higher compared to the observations at the longitudinal center. Also, Stretched_G correctly predicts the width of the squall line.

For Hurricane Harvey, its track (defined by the location of minimum sea level pressure) is accurately predicted by the Stretched_G simulation (Fig. 8c). Similar to that shown in Fig. 8b, the 24-h radar reflectivity composite of the inner-core to outer-core cross section through Hurricane Harvey is shown in Fig. 8d. The model predicts a larger hurricane eye compared to the observations. This can be improved

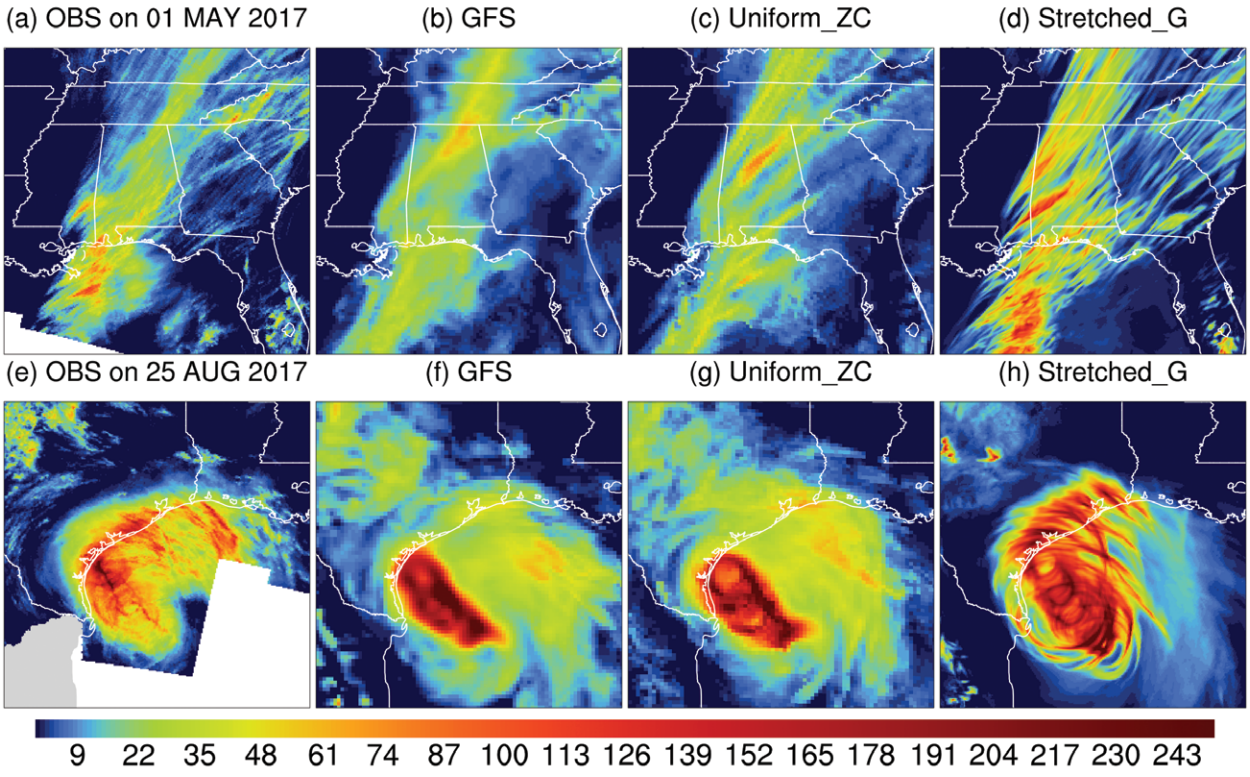

Fig. 9. Daily accumulated precipitation (mm) from (a),(e) Stage IV; (b),(f) GFS; (c),(g) Uniform_ZC; and (d),(h) Stretched_G on (a)–(d) 1 May and (e)–(h) 25 Aug 2017.

by using a less diffusive positive-definite tracer advection option in the dynamical core (figure not shown). Although Stretched_G produces a narrowed extent of the eyewall convection, it substantially overpredicts the radar reflectivity in the 2° radial band.

Finally, the daily accumulated precipitation for the GFS, Uniform_ZC, and Stretched_G forecasts are compared to the Stage IV observations (Fig. 9). For the squall line case, both the GFS and the two fvGFS versions correctly predict the northeastward movement of the convective systems. However, the GFS and Uniform_ZC do not predict the large amount of accumulated precipitation over the Mississippi Gulf Coast. By contrast, Stretched_G shows a finer-scale detail of strong convective storms in that area, although the precipitation is overpredicted compared to the observations. Stretched_G is the only one of the three models that clearly resolves small-scale structures of the convective activity both in the eyewall and in the rainbands extending to the northeast of Harvey near the coast of Texas and Louisiana. However, the precipitation is again overpredicted.

CONCLUSIONS AND DISCUSSION.

This study demonstrates the use of a simple variable-resolution technique to enable the Next Generation Global Prediction System (NGGPS) to efficiently represent convective-scale features in a global model, taking advantage of the enhanced capabilities provided by the modern dynamical core and an advanced microphysics scheme. As a milestone of the NGGPS development, the prototype of NGGPS developed at GFDL, called fvGFS, is presented in detail to provide a reference for future research and possible operational model development. The convection-permitting capability in the fvGFS is realized through a variable-resolution nonhydrostatic dynamical core and an upgraded cloud microphysics scheme, which are lacking in the current operational GFS. Evaluating 145 ten-day forecasts over a 2-yr period, we found that the predictive skill of the large-scale circulation in the 4–45 km variable-resolution fvGFS with GFDL cloud microphysics is comparable to that of the GFS. Improvements in convective-scale prediction are clearly demonstrated with the new modeling system, despite the lack of scale-aware physical parameterizations, especially for cumulus convection in the coarse-resolution domain.

The primary findings from this study are as follows. First, the large-scale forecast skill of the variable-resolution fvGFS is comparable to that

of the GFS in the Northern Hemisphere and is improved over the CONUS region when the GFDL cloud microphysics is used. Second, the variable-resolution fvGFS improves the representation of CONUS orographic precipitation, the forecast skill of light and heavy precipitation, and the phase and amplitude of the diurnal cycle of precipitation, compared to the 13-km uniform-resolution fvGFS and the operational GFS. The variable-resolution fvGFS most accurately predicts the observed frequency of heavy to extreme precipitation in the SGP region. Finally, in two case studies, a squall line and Hurricane Harvey, the variable-resolution fvGFS more accurately simulates the size and intensity of convective-scale storms compared to the GFS and the uniform-resolution fvGFS with better predictions of convective rainfall.

However, there remain some limitations with this early version of the variable-resolution fvGFS that need to be addressed in the future. First, the skill of the 500-hPa geopotential height over the Southern Hemisphere degrades to a certain extent compared to the GFS. This suggests that the current physical parameterization package is only partially scale aware. This issue is being addressed in updates to the SAS convection scheme (Han et al. 2017) and other parameterizations. Second, orographic precipitation along the U.S. West Coast is still poorly simulated, and there is only a small improvement of precipitation forecast skill with increasing resolution. Both issues can be addressed by using better microphysics and convective schemes, and by considerations of the impact of subgrid terrain on the microphysics. Third, the GFDL MP is able to reduce the light precipitation biases but has less impact in improving the prediction of moderate to heavy precipitation. Moreover, the diurnal cycle of precipitation still has a considerable bias over the central CONUS and will require reconfiguring of the convective scheme (or using a scale-aware scheme) to realize systematic improvement (Davis et al. 2003; Clark et al. 2007). Increasing resolution allows the model to resolve precipitating convective structures more explicitly (Yu et al. 2014; Landu et al. 2014), but the variable-resolution fvGFS appears to overpredict the intensity of convective features.

Replacing the GFS spectral core with the FV3 dynamical core lays the foundation for future improvements in NGGPS, through its nonhydrostatic and variable-resolution capabilities among other features. However, the improvement to forecast skill by merely changing the dynamical core is limited. The errors in the initial conditions and from the physical parameterizations dominate forecast errors in the 13-km simulations. While the convective-scale prediction skill over the CONUS is improved in the stretched-grid model, especially when the GFDL microphysical scheme is incorporated, the variable-resolution grid, with gridcell widths varying from 4 to 45 km, leads to a degradation in large-scale prediction skill. This is not surprising given that the current GFS physics, including the convective scheme, boundary layer scheme, and gravity wave drag scheme are not effectively scale aware and are tuned for the current operational 13-km resolution. When the grid is locally refined to 4 km, the model enters the so-called planetary boundary layer gray zone (Wyngaard 2004), and the current GFS physics parameterizations may not optimally represent either the high-resolution area or the lower-resolution area on the opposite side of Earth. More sophisticated cloud microphysics allows for a better simulation of mesoscale circulation and precipitation, which results in overall improvements in the large-scale and mesoscale simulations. To further improve the forecast skill in the variable-resolution model, scale-aware physical parameterizations, which are currently being developed at GFDL, NCEP, and elsewhere, are required.

The grid stretching ability of the fvGFS model provides a powerful and user-friendly way to develop and test scale-aware physical parameterizations. The conceptual simplicity of the stretched-grid approach and its ability to efficiently reach convective-scale resolutions are beneficial to most users of FV3-based models (e.g., fvGFS, GFDL Atmospheric Model, Goddard Earth Observing System Model, Community Earth System Model), even for researchers whose technical support and computational resources are limited. The grid stretching capability will soon be made available in the NGGPS for community use as well.

ACKNOWLEDGMENTS. The authors thank the following people who contributed to the fvGFS and NGGPS. Rusty Benson built the interface for coupling the FV3 to the GFS physics and maintained the model infrastructure. Zhi Liang built the preprocessing, postprocessing, remapping packages, and the message passing infrastructure. Tim Marchok and Matt Morin prepared the GFS forecast datasets. The authors thank Ming Zhao, Baoqiang Xiang, Andy Hazelton, Morris Bender, Tim Marchok, Bill Stern, Peng Li, and Wenhao Zhou for reviewing this manuscript. The authors also benefited from discussions with Mingjing Tong on radar reflectivity. The authors appreciate the three anonymous reviewers and Dr. Nigel Wood for their insightful comments that led to a significant improvement of the manuscript. This study was supported by the Sandy Supplemental and NGGPS

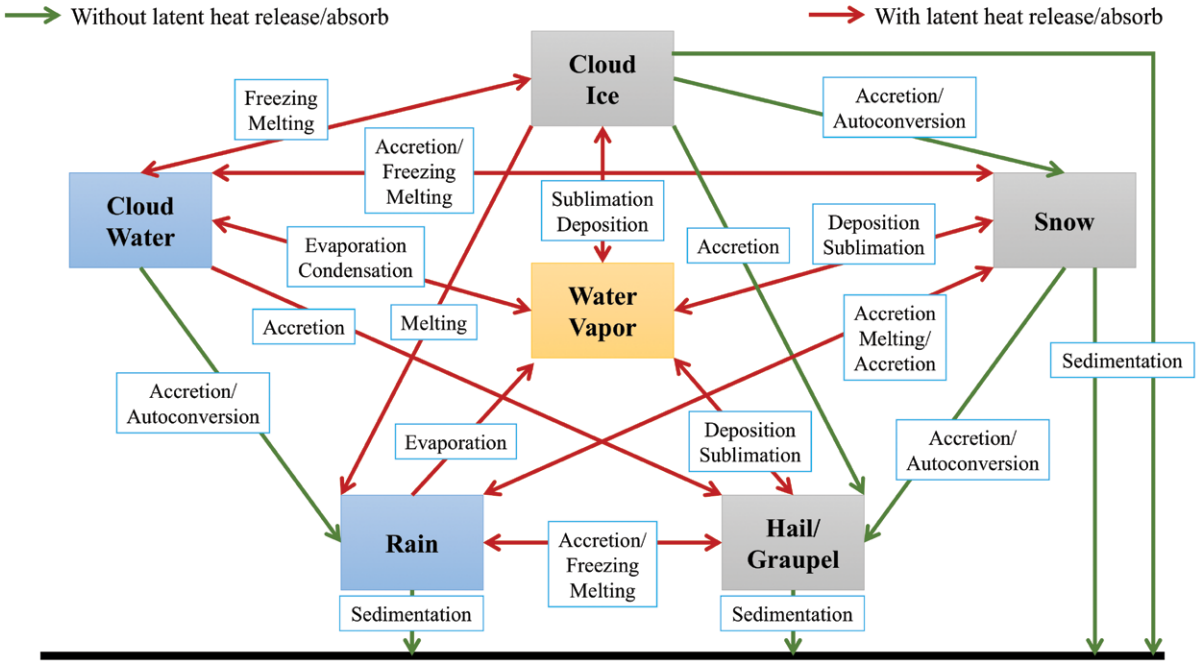

Fig. A1. Schematic of the GFDL cloud microphysics. The yellow box indicates prognostic water vapor, blue boxes indicate prognostic liquid phase water species, and gray boxes indicate prognostic solid phase water species. Red arrows indicate processes involving heating/cooling from phase changes, while green arrows indicate conversion and sedimentation processes.

project. ERA-Interim reanalysis data are available from the European Centre for Medium-Range Weather Forecasts (ECMWF) at www.ecmwf.int/. NCEP reanalysis data are available from NOAA Earth System Research Laboratory at www.esrl.noaa.gov/. Stage IV radar-derived precipitation data are available from NCEP Environmental Modeling Center (EMC) at www.emc.ncep.noaa.gov/. Observed radar reflectivity data are available from NOAA National Centers for Environmental Information (NCEI) at www.ncei.noaa.gov/.

APPENDIX: GFDL CLOUD MICROPHYSICS. GFDL developed the single-moment 6-category cloud microphysics based on the Lin–Lord–Krueger cloud microphysics (Lin et al. 1983; Lord et al. 1984; Krueger et al. 1995) formerly used in the GFDL ZETAC regional model (Pauluis and Garner 2006). It has been substantially revised and designed for the GFDL global cloud-resolving model HiRAM (High-Resolution Atmospheric Model; Chen and Lin 2011, 2013; Harris et al. 2016), and continually developed and maintained by Dr. Shian-Jiann Lin and his team since the early 2000s. The schematic of the GFDL cloud microphysics is shown in Fig. A1.

Along with the GFDL Finite-Volume Cubed-Sphere Dynamical Core (FV3), the model configuration with the GFDL cloud microphysics has the following unique attributes:

1) Fast-time scale cloud processes (currently phase changes and latent heating) are embedded within the Lagrangian-to-Eulerian remapping in the FV3 dynamical core and can be updated more rapidly than the rest of the physics.
2) Time-splitting is applied between warm-rain and ice-phase processes, with the warm rain called at twice the frequency.
3) Time-implicit monotonic scheme and piecewise parabolic method are applied for the falling of condensates, ensuring shape preservation and stability without needing to subcycle.
4) Thermodynamic consistency is maintained between the dynamics and the physics by considering the heat content of the condensates. The total moist energy is precisely conserved within the cloud microphysics.
5) Condensates carry heat and momentum during the sedimentation processes.
6) Scale awareness is achieved by an assumed horizontal subgrid variability and a second-order finite-volume-type vertical reconstruction for autoconversion processes.

REFERENCES

Arakawa, A., 2004: The cumulus parameterization problem: Past, present, and future. *J. Climate*, **17**, 2493–2525, https://doi.org/10.1175/1520-0442(2004)017<2493:RATCPP>2.0.CO;2.

Baldauf, M., A. Seifert, J. Forstner, D. Majewski, M. Raschendorfer, and T. Reinhardt, 2011: Operational convective-scale numerical weather prediction with the COSMO model: Description and sensitivities. *Mon. Wea. Rev.*, **139**, 3887–3905, https://doi.org/10.1175/MWR-D-10-05013.1.

Bechtold, P., N. Semane, P. Lopez, J. P. Chaboureau, A. Beljaars, and N. Bormann, 2014: Representing equilibrium and nonequilibrium convection in large-scale models. *J. Atmos. Sci.*, **71**, 734–753, https://doi.org/10.1175/JAS-D-13-0163.1.

Bryan, G. H., and H. Morrison, 2012: Sensitivity of a simulated squall line to horizontal resolution and parameterization of microphysics. *Mon. Wea. Rev.*, **140**, 202–225, https://doi.org/10.1175/MWR-D-11-00046.1.

——, J. C. Wyngaard, and J. M. Fritsch, 2003: Resolution requirements for the simulation of deep moist convection. *Mon. Wea. Rev.*, **131**, 2394–2416, https://doi.org/10.1175/1520-0493(2003)131<2394:RRFTSO>2.0.CO;2.

Chen, J. H., and S. J. Lin, 2011: The remarkable predictability of inter-annual variability of Atlantic hurricanes during the past decade. *Geophys. Res. Lett.*, **38**, L11804, https://doi.org/10.1029/2011GL047629.

——, and ——, 2013: Seasonal predictions of tropical cyclones using a 25-km-resolution general circulation model. *J. Climate*, **26**, 380–398, https://doi.org/10.1175/JCLI-D-12-00061.1.

——, X. Chen, S. J. Lin, L. Magnusson, M. Bender, L. Zhou, and S. Rees, 2018: Tropical cyclones in GFDL fvGFS—Impacts of dycore, physics and initial conditions. *33rd Conf. on Hurricane and Tropical Meteorology*, Ponte Vedra, FL, Amer. Meteor. Soc., 9B.4, https://ams.confex.com/ams/33HURRICANE/webprogram/Paper339827.html.

——, and Coauthors, 2019: Advancements in hurricane prediction with NOAA's next-generation forecast system. *Geophys. Res. Lett.*, **46**, https://doi.org/10.1029/2019GL082410.

Chen, X., N. Andronova, B. Van Leer, J. E. Penner, J. P. Boyd, C. Jablonowski, and S. J. Lin, 2013: A control-volume model of the compressible Euler equations with a vertical Lagrangian coordinate. *Mon. Wea. Rev.*, **141**, 2526–2544, https://doi.org/10.1175/MWR-D-12-00129.1.

Chun, H.-Y., and J.-J. Baik, 1994: Weakly nonlinear response of a stably stratified atmosphere to diabatic forcing in a uniform flow. *J. Atmos. Sci.*, **51**, 3109–3121, https://doi.org/10.1175/1520-0469(1994)051<3109:WNROAS>2.0.CO;2.

Clark, A. J., W. A. Gallus, and T. C. Chen, 2007: Comparison of the diurnal precipitation cycle in convection-resolving and non-convection-resolving mesoscale models. *Mon. Wea. Rev.*, **135**, 3456–3473, https://doi.org/10.1175/MWR3467.1.

——, ——, M. Xue, and F. Y. Kong, 2009: A comparison of precipitation forecast skill between small convection-allowing and large convection-parameterizing ensembles. *Wea. Forecasting*, **24**, 1121–1140, https://doi.org/10.1175/2009WAF2222222.1.

Clark, P., N. Roberts, H. Lean, S. P. Ballard, and C. Charlton-Perez, 2016: Convection-permitting models: A step-change in rainfall forecasting. *Meteor. Appl.*, **23**, 165–181, https://doi.org/10.1002/met.1538.

Clough, S. A., M. W. Shephard, E. J. Mlawer, J. S. Delamere, M. J. Iacono, K. Cady-Pereira, S. Boukabara, and P. D. Brown, 2005: Atmospheric radiative transfer modeling: A summary of the AER codes. *J. Quant. Spectrosc. Radiat. Transfer*, **91**, 233–244, https://doi.org/10.1016/j.jqsrt.2004.05.058.

Davis, C. A., K. W. Manning, R. E. Carbone, S. B. Trier, and J. D. Tuttle, 2003: Coherence of warm-season continental rainfall in numerical weather prediction models. *Mon. Wea. Rev.*, **131**, 2667–2679, https://doi.org/10.1175/1520-0493(2003)131<2667:COWCRI>2.0.CO;2.

Dee, D. P., and Coauthors, 2011: The ERA-Interim reanalysis: Configuration and performance of the data assimilation system. *Quart. J. Roy. Meteor. Soc.*, **137**, 553–597, https://doi.org/10.1002/qj.828.

Done, J., C. A. Davis, and M. Weisman, 2004: The next generation of NWP: Explicit forecasts of convection using the Weather Research and Forecasting (WRF) Model. *Atmos. Sci. Lett.*, **5**, 110–117, https://doi.org/10.1002/asl.72.

Eckermann, S., 2009: Hybrid σ–p coordinate choices for a global model. *Mon. Wea. Rev.*, **137**, 224–245, https://doi.org/10.1175/2008MWR2537.1.

Ek, M. B., K. E. Mitchell, Y. Lin, E. Rogers, P. Grunmann, V. Koren, G. Gayno, and J. D. Tarpley, 2003: Implementation of Noah land surface model advances in the National Centers for Environmental Prediction operational mesoscale Eta model. *J. Geophys. Res.*, **108**, 8851, https://doi.org/10.1029/2002JD003296.

Fox-Rabinovitz, M., J. Cote, B. Dugas, M. Deque, and J. L. McGregor, 2006: Variable resolution general circulation models: Stretched-grid model intercomparison project (SGMIP). *J. Geophys. Res.*, **111**, D16104, https://doi.org/10.1029/2005JD006520.

Fudeyasu, H., Y. Q. Wang, M. Satoh, T. Nasuno, H. Miura, and W. Yanase, 2008: Global cloud-system-resolving model NICAM successfully simulated the lifecycles of two real tropical cyclones. *Geophys. Res. Lett.*, **35**, L22808, https://doi.org/10.1029/2008GL036003.

Gesch, D. B., K. L. Verdin, and S. K. Greenlee, 1999: New land surface digital elevation model covers the Earth. *Eos, Trans. Amer. Geophys. Union*, **80**, 69–70, https://doi.org/10.1029/99EO00050.

Grams, J. S., R. L. Thompson, D. V. Snively, J. A. Prentice, G. M. Hodges, and L. J. Reames, 2012: A climatology and comparison of parameters for significant tornado events in the United States. *Wea. Forecasting*, **27**, 106–123, https://doi.org/10.1175/WAF-D-11-00008.1.

Hamill, T. M., 1999: Hypothesis tests for evaluating numerical precipitation forecasts. *Wea. Forecasting*, **14**, 155–167, https://doi.org/10.1175/1520-0434(1999)014<0155:HTFENP>2.0.CO;2.

Han, J., and H. L. Pan, 2011: Revision of convection and vertical diffusion schemes in the NCEP Global Forecast System. *Wea. Forecasting*, **26**, 520–533, https://doi.org/10.1175/WAF-D-10-05038.1.

——, M. L. Witek, J. Teixeira, R. Sun, H. L. Pan, J. K. Fletcher, and C. S. Bretherton, 2016: Implementation in the NCEP GFS of a hybrid eddy-diffusivity mass-flux (EDMF) boundary layer parameterization with dissipative heating and modified stable boundary layer mixing. *Wea. Forecasting*, **31**, 341–352, https://doi.org/10.1175/WAF-D-15-0053.1.

——, W. G. Wang, Y. C. Kwon, S. Y. Hong, V. Tallapragada, and F. L. Yang, 2017: Updates in the NCEP GFS cumulus convection schemes with scale and aerosol awareness. *Wea. Forecasting*, **32**, 2005–2017, https://doi.org/10.1175/WAF-D-17-0046.1.

Harris, L. M., and S. J. Lin, 2013: A two-way nested global-regional dynamical core on the cubed-sphere grid. *Mon. Wea. Rev.*, **141**, 283–306, https://doi.org/10.1175/MWR-D-11-00201.1.

——, ——, and C. Y. Tu, 2016: High-resolution climate simulations using GFDL HiRAM with a stretched global grid. *J. Climate*, **29**, 4293–4314, https://doi.org/10.1175/JCLI-D-15-0389.1.

Hazelton, A. T., M. Bender, M. Morin, L. Harris, and S.-J. Lin, 2018a: 2017 Atlantic hurricane forecasts from a high-resolution version of the GFDL fvGFS model: Evaluation of track, intensity, and structure. *Wea. Forecasting*, **33**, 1317–1337, https://doi.org/10.1175/WAF-D-18-0056.1.

——, L. Harris, and S. J. Lin, 2018b: Evaluation of tropical cyclone structure forecasts in a high-resolution version of the multiscale GFDL fvGFS model. *Wea. Forecasting*, **33**, 419–442, https://doi.org/10.1175/WAF-D-17-0140.1.

Jolliffe, I. T., and D. B. Stephenson, 2003: *Forecast Verification: A Practitioner's Guide in Atmospheric Science*. John Wiley and Sons, 274 pp.

Juang, H. M. H., 1992: A spectral fully compressible nonhydrostatic mesoscale model in hydrostatic sigma coordinates: Formulation and preliminary results. *Meteor. Atmos. Phys.*, **50**, 75–88, https://doi.org/10.1007/BF01025506.

——, 2004: A reduced spectral transform for the NCEP seasonal forecast global spectral atmospheric model. *Mon. Wea. Rev.*, **132**, 1019–1035, https://doi.org/10.1175/1520-0493(2004)132<1019:ARSTFT>2.0.CO;2.

——, 2008: Mass conserving positive definite semi-Lagrangian advection in NCEP GFS: Decomposition of massively parallel computing without halo. *13th Workshop on Use of High Performance Computing in Meteorology*, Reading, United Kingdom, ECMWF, 50 pp., www.ecmwf.int/sites/default/files/elibrary/2008/15346-mass-conserving-and-positive-definite-semi-lagrangian-advection-ncep-gfs-decomposition.pdf.

Kalnay, E., 2003: *Atmospheric Modeling, Data Assimilation and Predictability*. Cambridge University Press, 369 pp.

——, and Coauthors, 1996: The NCEP/NCAR 40-Year Reanalysis Project. *Bull. Amer. Meteor. Soc.*, **77**, 437–471, https://doi.org/10.1175/1520-0477(1996)077<0437:TNYRP>2.0.CO;2.

Kim, Y.-J., and A. Arakawa, 1995: Improvement of orographic gravity wave parameterization using a mesoscale gravity wave model. *J. Atmos. Sci.*, **52**, 1875–1902, https://doi.org/10.1175/1520-0469(1995)052<1875:IOOGWP>2.0.CO;2.

——, and J. D. Doyle, 2005: Extension of an orographic-drag parametrization scheme to incorporate orographic anisotropy and flow blocking. *Quart. J. Roy. Meteor. Soc.*, **131**, 1893–1921, https://doi.org/10.1256/qj.04.160.

Krueger, S. K., Q. A. Fu, K. N. Liou, and H. N. S. Chin, 1995: Improvements of an ice-phase microphysics parameterization for use in numerical simulations of tropical convection. *J. Appl. Meteor.*, **34**, 281–287, https://doi.org/10.1175/1520-0450-34.1.281.

Landu, K., L. R. Leung, S. Hagos, V. Vinoj, S. A. Rauscher, T. Ringler, and M. Taylor, 2014: The dependence of ITCZ structure on model resolution and dynamical core in aquaplanet simulations. *J. Climate*, **27**, 2375–2385, https://doi.org/10.1175/JCLI-D-13-00269.1.

Leung, L. R., and S. J. Ghan, 1998: Parameterizing subgrid orographic precipitation and surface cover in climate models. *Mon. Wea. Rev.*, **126**, 3271–3291, https://doi.org/10.1175/1520-0493(1998)126<3271:PSOPAS>2.0.CO;2.

Li, X., C. H. Sui, K. M. Lau, and W. K. Tao, 2005: Tropical convective responses to microphysical and radiative processes: A sensitivity study with a 2-D cloud resolving model. *Meteor. Atmos. Phys.*, **90**, 245–259, https://doi.org/10.1007/s00703-004-0088-5.

Lin, S.-J., 1997: A finite-volume integration method for computing pressure gradient force in general vertical coordinates. *Quart. J. Roy. Meteor. Soc.*, **123**, 1749–1762, https://doi.org/10.1002/qj.49712354214.

——, 2004: A "vertically Lagrangian" finite-volume dynamical core for global models. *Mon. Wea. Rev.*, **132**, 2293–2307, https://doi.org/10.1175/1520-0493(2004)132<2293:AVLFDC>2.0.CO;2.

——, 2018: Preliminary evaluation of systematic biases in a FV3-powered global cloud-permitting model. *Fifth ENES HPC Workshop on HPC for High-Resolution Weather and Climate Modeling*, Lecce, Italy, ESiWACE, 22 pp., www.esiwace.eu/events/5th-enes-hpc-workshop/presentations/lin-fv3.

Lin, Y., 2011: GCIP/EOP Surface: Precipitation NCEP/EMC 4KM Gridded Data (GRIB) Stage IV Data, version 1.0. UCAR/NCAR Earth Observing Laboratory, accessed 15 May 2017, https://doi.org/10.5065/D6PG1QDD.

Lin, Y.-L., R. D. Farley, and H. D. Orville, 1983: Bulk parameterization of the snow field in a cloud model. *J. Climate Appl. Meteor.*, **22**, 1065–1092, https://doi.org/10.1175/1520-0450(1983)022<1065:BPOTSF>2.0.CO;2.

Lord, S. J., H. E. Willoughby, and J. M. Piotrowicz, 1984: Role of a parameterized ice-phase microphysics in an axisymmetric, nonhydrostatic tropical cyclone model. *J. Atmos. Sci.*, **41**, 2836–2848, https://doi.org/10.1175/1520-0469(1984)041<2836:ROAPIP>2.0.CO;2.

Mason, S. J., and N. E. Graham, 1999: Conditional probabilities, relative operating characteristics, and relative operating levels. *Wea. Forecasting*, **14**, 713–725, https://doi.org/10.1175/1520-0434(1999)014<0713:CPROCA>2.0.CO;2.

Mass, C. F., D. Ovens, K. Westrick, and B. A. Colle, 2002: Does increasing horizontal resolution produce more skillful forecasts? *Bull. Amer. Meteor. Soc.*, **83**, 407–430, https://doi.org/10.1175/1520-0477(2002)083<0407:DIHRPM>2.3.CO;2.

McGregor, J. L., 2015: Recent developments in variable-resolution global climate modelling. *Climatic Change*, **129**, 369–380, https://doi.org/10.1007/s10584-013-0866-5.

Miura, H., M. Satoh, T. Nasuno, A. T. Noda, and K. Oouchi, 2007: A Madden-Julian oscillation event realistically simulated by a global cloud-resolving model. *Science*, **318**, 1763–1765, https://doi.org/10.1126/science.1148443.

Miyamoto, Y., Y. Kajikawa, R. Yoshida, T. Yamaura, H. Yashiro, and H. Tomita, 2013: Deep moist atmospheric convection in a subkilometer global simulation. *Geophys. Res. Lett.*, **40**, 4922–4926, https://doi.org/10.1002/grl.50944.

Müller, M., and Coauthors, 2017: AROME-MetCoOp: A Nordic convective-scale operational weather prediction model. *Wea. Forecasting*, **32**, 609–627, https://doi.org/10.1175/WAF-D-16-0099.1.

Murphy, A. H., and E. S. Epstein, 1989: Skill scores and correlation-coefficients in model verification. *Mon. Wea. Rev.*, **117**, 572–581, https://doi.org/10.1175/1520-0493(1989)117<0572:SSACCI>2.0.CO;2.

Pauluis, O., and S. Garner, 2006: Sensitivity of radiative-convective equilibrium simulations to horizontal resolution. *J. Atmos. Sci.*, **63**, 1910–1923, https://doi.org/10.1175/JAS3705.1.

Petch, J. C., 2006: Sensitivity studies of developing convection in a cloud-resolving model. *Quart. J. Roy. Meteor. Soc.*, **132**, 345–358, https://doi.org/10.1256/qj.05.71.

Prein, A. F., and Coauthors, 2015: A review on regional convection-permitting climate modeling: Demonstrations, prospects, and challenges. *Rev. Geophys.*, **53**, 323–361, https://doi.org/10.1002/2014RG000475.

Putman, W. M., and S. H. Lin, 2007: Finite-volume transport on various cubed-sphere grids. *J. Comput. Phys.*, **227**, 55–78, https://doi.org/10.1016/j.jcp.2007.07.022.

——, and M. Suarez, 2011: Cloud-system resolving simulations with the NASA Goddard Earth Observing System global atmospheric model (GEOS-5). *Geophys. Res. Lett.*, **38**, L16809, https://doi.org/10.1029/2011GL048438.

Randall, D. A., 2013: Beyond deadlock. *Geophys. Res. Lett.*, **40**, 5970–5976, https://doi.org/10.1002/2013GL057998.

Roberts, N. M., and H. W. Lean, 2008: Scale-selective verification of rainfall accumulations from high-resolution forecasts of convective events. *Mon. Wea. Rev.*, **136**, 78–97, https://doi.org/10.1175/2007MWR2123.1.

Satoh, M., T. Matsuno, H. Tomita, H. Miura, T. Nasuno, and S. Iga, 2008: Nonhydrostatic icosahedral atmospheric model (NICAM) for global cloud resolving simulations. *J. Comput. Phys.*, **227**, 3486–3514, https://doi.org/10.1016/j.jcp.2007.02.006.

Schumacher, R. S., and A. J. Clark, 2014: Evaluation of ensemble configurations for the analysis and prediction of heavy-rain-producing mesoscale convective systems. *Mon. Wea. Rev.*, **142**, 4108–4138, https://doi.org/10.1175/MWR-D-13-00357.1.

Schwartz, C. S., and Coauthors, 2010: Toward improved convection-allowing ensembles: Model physics sensitivities and optimizing probabilistic guidance with small ensemble membership. *Wea. Forecasting*, **25**, 263–280, https://doi.org/10.1175/2009WAF2222267.1.

Sela, J. G., 1980: Spectral modeling at the National Meteorological Center. *Mon. Wea. Rev.*, **108**, 1279–1292, https://doi.org/10.1175/1520-0493(1980)108<1279:SMATNM>2.0.CO;2.

Sobash, R. A., J. S. Kain, D. R. Bright, A. R. Dean, M. C. Coniglio, and S. J. Weiss, 2011: Probabilistic forecast guidance for severe thunderstorms based on the identification of extreme phenomena in convection-allowing model forecasts. *Wea. Forecasting*, **26**, 714–728, https://doi.org/10.1175/WAF-D-10-05046.1.

Staniforth, A., 1997: Regional modeling: A theoretical discussion. *Meteor. Atmos. Phys.*, **63**, 15–29, https://doi.org/10.1007/BF01025361.

Stensrud, D. J., and Coauthors, 2009: Convective-scale warn-on-forecast system: A vision for 2020. *Bull. Amer. Meteor. Soc.*, **90**, 1487–1499, https://doi.org/10.1175/2009BAMS2795.1.

Stephan, K., S. Klink, and C. Schraff, 2008: Assimilation of radar-derived rain rates into the convective-scale model COSMO-DE at DWD. *Quart. J. Roy. Meteor. Soc.*, **134**, 1315–1326, https://doi.org/10.1002/qj.269.

Stoelinga, M. T., 2005: Simulated equivalent reflectivity factor as currently formulated in RIP: Description and possible improvements. University of Washington Tech. Rep., 5 pp., http://citeseerx.ist.psu.edu/viewdoc/download?doi=10.1.1.522.925&rep=rep1&typepdf.

Warner, T. T., R. A. Peterson, and R. E. Treadon, 1997: A tutorial on lateral boundary conditions as a basic and potentially serious limitation to regional numerical weather prediction. *Bull. Amer. Meteor. Soc.*, **78**, 2599–2617, https://doi.org/10.1175/1520-0477(1997)078<2599:ATOLBC>2.0.CO;2.

Weisman, M. L., W. C. Skamarock, and J. B. Klemp, 1997: The resolution dependence of explicitly modeled convective systems. *Mon. Wea. Rev.*, **125**, 527–548, https://doi.org/10.1175/1520-0493(1997)125<0527:TRDOEM>2.0.CO;2.

——, C. Davis, W. Wang, K. W. Manning, and J. B. Klemp, 2008: Experiences with 0–36-h explicit convective forecasts with the WRF-ARW Model. *Wea. Forecasting*, **23**, 407–437, https://doi.org/10.1175/2007WAF2007005.1.

Wyngaard, J. C., 2004: Toward numerical modeling in the "terra incognita." *J. Atmos. Sci.*, **61**, 1816–1826, https://doi.org/10.1175/1520-0469(2004)061<1816:TNMITT>2.0.CO;2.

Xue, M., F. Kong, K. W. Thomas, J. Gao, Y. Wang, K. Brewster, and K. K. Droegemeier, 2013: Prediction of convective storms at convection-resolving 1 km resolution over continental United States with radar data assimilation: An example case of 26 May 2008 and precipitation forecasts from spring 2009. *Adv. Meteor.*, **2013**, 259052, https://doi.org/10.1155/2013/259052.

Yang, F., 2009: On the negative water vapor in the NCEP GFS: Sources and solution. *23rd Conf. on Weather Analysis and Forecasting/19th Conf. on Numerical Weather Prediction*, Omaha, NE, Amer. Meteor. Soc., JP1.1, https://ams.confex.com/ams/23WAF19NWP/techprogram/paper_152548.htm.

Yano, J.-I., and Coauthors, 2018: Scientific challenges of convective-scale numerical weather prediction. *Bull. Amer. Meteor. Soc.*, **99**, 699–710, https://doi.org/10.1175/BAMS-D-17-0125.1.

Yu, H., Q. Bao, L. Zhou, X. Wang, and Y. Liu, 2014: Sensitivity of precipitation in aqua-planet experiments with an AGCM. *Atmos. Ocean. Sci. Lett.*, **7**, 1–6, https://doi.org/10.3878/j.issn.1674-2834.13.0033.

Zhao, Q. Y., and F. H. Carr, 1997: A prognostic cloud scheme for operational NWP models. *Mon. Wea. Rev.*, **125**, 1931–1953, https://doi.org/10.1175/1520-0493(1997)125<1931:APCSFO>2.0.CO;2.

Zhou, L. J., and Coauthors, 2015: Global energy and water balance: Characteristics from Finite-Volume Atmospheric Model of the IAP/LASG (FAMIL1). *J. Adv. Model. Earth Syst.*, **7**, 1–20, https://doi.org/10.1002/2014MS000349.

Attention AMS Student Members

Stay connected to AMS after graduation for half the regular membership rate

AMS
American Meteorological Society

Let AMS help you build your expertise, your network, your career. There's never been a more important time to be a member.

http://www.ametsoc.org/earlycareer